Fixed-Structure, Low-Order Damping and Tracking Control Schemes for Nanopositioning ⋆

Arnfinn A. Eielsen * **Marialena Vagia** * **J. Tommy Gravdahl** *
Kristin Y. Pettersen *

* *Dept. of Engineering Cybernetics, Norwegian Univ. of Science and Technology, Trondheim, Norway*
(e-mail: {eielsen,marialev,tomgra,kyp}@itk.ntnu.no).

Abstract: Fast and accurate tracking of periodic reference trajectories is highly desirable in many nanopositioning applications, including scanning probe microscopy. Performance in common positioning stage designs is limited by the presence of lightly damped resonances, and actuator nonlinearities such as hysteresis and creep. To improve the tracking performance in such systems, several damping and tracking control schemes have been presented in the literature. In this paper, five different control schemes are presented and applied to a nanopositioning system for experimental comparison. They include schemes applying damping control in the form of positive position feedback, integral resonant control, integral force feedback, and passive shunt-damping. Also, a control scheme requiring only a combination of a low-pass filter and an integrator is presented. The control schemes are fixed-structure, low-order control laws, for which few results exist in the literature with regards to optimal tuning. A practical tuning procedure for obtaining good tracking performance for all of the presented control schemes is therefore presented. The schemes provide similar performance, and the main differences are due to the specific implementation of each scheme.

Keywords: Micro-/Nanosystems; Motion Control; Actuator and Sensor Systems

1. INTRODUCTION

Nanopositioning devices are used for high-resolution positioning, including, but not limited to, scanning probe microscopy and its many applications for imaging and manipulation. Some tasks require periodic reference trajectory tracking, typically for imaging, while other tasks require arbitrary reference trajectory tracking, such as for manipulation, fabrication, and lithography. In order to improve throughput in such settings, high bandwidth control is required (Salapaka and Salapaka, 2008; Clayton et al., 2009; Devasia et al., 2007).

Most high-speed nanopositioning devices use piezoelectric actuators, as they produce large forces and provide friction-less motion. As such, they are ideal for high-speed, high-resolution positioning. A positioning device applying piezoelectric actuators typically exhibit lightly damped resonances. This is a disadvantage, as it limits the usable bandwidth because reference signals with high frequency components will excite the vibration modes, prohibiting accurate positioning. It also makes the device susceptible to environmental disturbances, such as sound and floor vibrations. The hysteresis and creep non-linearities in piezoelectric actuators is an additional challenge. These are loss-phenomena that prevent the system from having a linear response, introducing bounded input disturbances dependent on the driving voltage signal (Devasia et al., 2007). There also exist several sources of dynamic uncertainty. Hysteresis, in addition to introducing an input disturbance, change the effective gain of the actuator depending on the amplitude of the driving voltage signal. Actuator gain is also dependent on temperature, and reduces over time due to depolarization (Bertotti and Mayergoyz, 2005, Ch. 4). In addition, users typically need to position payloads of various masses, thus resonant frequencies and the effective gain of the mechanical structure change as a result.

Tracking control for nanopositioning devices can be achieved using feed-forward and feedback control techniques. Although feed-forward techniques can provide very good results (Clayton et al., 2009), feedback control may be necessary in order to reduce sensitivity to uncertainty and disturbances. In order to control lightly damped vibrational modes in active structures, several control schemes that introduce damping have been developed. These include fixed-structure, low-order control laws, such as positive position feedback (Fanson and Caughey, 1990), integral force feedback (Preumont et al., 1992), passive shunt-damping (Hagood and von Flotow, 1991), resonant control (Pota et al., 2002) and integral resonant control (Aphale et al., 2007). By coupling such schemes with an integral control law, significantly better reference tracking performance can be achieved. With the exception of passive shunt-damping, this has been experimentally demonstrated in Aphale et al. (2008); Fleming et al. (2010); Fleming (2010). The main reason for the increased performance, is that a reduction of the dominant resonant peak of the system leads to an increased gain margin, enabling a higher gain to be used for the reference tracking integral control law (Fleming, 2010).

General model based control laws can also be used, such as $\mathcal{H}_\infty$-synthesis (Skogestad and Postlethwaite, 2005), linear-

⋆ This work was supported by the Norwegian University of Science and Technology and the Norwegian Research Council, and parts of this work was carried out during the tenure of an ERCIM "Alain Bensoussan" Fellowship Programme. This Programme is supported by the Marie Curie Co-Funding of Regional, National and International Programmes (COFUND) of the European Commission.

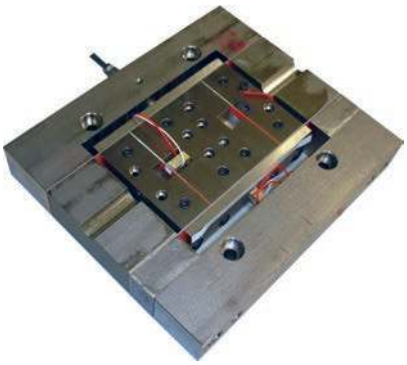

Fig. 1. Custom flexure-guided nanopositioning stage.

quadratic-gaussian regulator (Goodwin et al., 2000), or output feedback control laws such as pole-placement and model reference control (Ioannou and Sun, 1995). The advantage of using fixed-structure, low-order control laws is mostly practical, as such control laws are simple to implement and have low computational complexity. This allows for the highest possible sampling frequency when implementing using digital signal processing equipment, which will reduce the noise floor due to sampling and quantization in the analog-to-digital converter (Lyons, 2010). The simplicity also makes them feasible for implementation using analog circuit elements. This can be beneficial, as it avoids noise due to sampling and quantization altogether. The disadvantage of using fixed-structure, low-order control laws, is a lack of methods for optimal tuning, which is a long standing and challenging control engineering problem.

1.1 Contributions

Five different damping and tracking control schemes are presented and applied to a nanopositioning system for experimental comparison. All the schemes combine integral action with a control law that introduces damping of the dominant vibration mode of the system. The damping control schemes considered, are positive position feedback (PPF), integral resonant control (IRC), integral force feedback (IFF), and passive shunt-damping (PSD).

A control scheme based on the work in Eielsen et al. (2011) is also presented, and the tuning methodology therein is generalized and also applied to the presented control schemes based on PPF, IRC, IFF, and PSD. IRC has been applied in Fleming et al. (2010), and IFF in Fleming (2010). PPF, as well as polynomial-based control, is applied in Aphale et al. (2008).

2. SYSTEM DESCRIPTION AND MODELING

2.1 Description of the Experimental System

The experimental set-up consists of a dSPACE DS1103 hardware-in-the-loop (HIL) system, an ADE 6810 capacitive gauge, an ADE 6501 capacitive probe from ADE Technologies, a Piezodrive PDX200 voltage amplifier, two SIM 965 programmable filters from Stanford Research Systems, and the custom-made long-range serial-kinematic nanopositioner shown in Fig. 1. The nanopositioner is fitted with a Noliac SCMAP07-H10 actuator, where one of the stack elements is used as a force transducer. The transducer current is measured using a Burr-Brown OPA2111 configured with a 10 kΩ resistor, thus having a sensitivity of -10 V/mA. The capacitive probe has a first-order response and a bandwidth of 100 kHz, and the voltage amplifier with the capacitive load of the actuator, has a first-order response and a bandwidth in excess of 100 kHz. The voltage amplifier is also fitted with a current monitor with a sensitivity of 1 V/A, which enables the current in the actuator circuit to be measured. The capacitive measurement has a sensitivity of $1/5$ V/μm and the voltage amplifier has a gain of 20 V/V. With the DS1103 board, a sampling frequency of $f_s = 100$ kHz is used for all the experiments. For numerical integration, a third-order Runge-Kutta scheme is used.

A diagram of the system used is shown in Fig. 2. The positioner dynamics is represented by $G_p(s)$, the amplifier and reconstruction filter dynamics by $W_r(s)$, and the sensor and anti-aliasing filter dynamics by $W_a(s)$. The signal u is the input generated by the digital-to-analog converter, y_m is the output from the anti-aliasing filter, n is the sensor noise, and w is the input disturbance, mostly caused by hysteresis, creep, and environmental vibration noise.

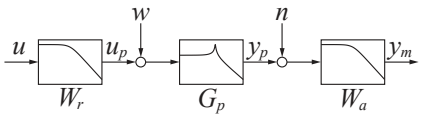

Fig. 2. System diagram.

2.2 Mechanical Model

The nanopositioning stage used is shown in Fig. 1. The serial-kinematic motion mechanism is designed to make the first vibration mode dominant and to occur in the actuation direction (piston mode). More details on the design of this stage can be found in Leang and Fleming (2009).

The displacement is generated using a piezoelectric actuator. Such actuators generate a force proportional to an applied voltage (Preumont, 2006). The applied external force from the piezoelectric actuator f_a (N) can be expressed as

$$f_a = e_a(u_a + w) \ , \tag{1}$$

where e_a (N V^{-1} = C N^{-1}) is the effective gain of the piezoelectric actuator from voltage to force, and u_a (V) is the applied voltage. Piezoelectric actuators introduce hysteresis and creep when driven by an external voltage signal. These effects occur in the electrical domain (Newcomb and Flinn, 1982), and it is a reasonable assumption to consider this behavior as a bounded disturbance added to the input, represented by the term w (V) (Stepanenko and Su, 1998).

The dynamics due to an applied voltage u_a or disturbance w of a point d (m) on the flexible structure, as observed by a co-located sensor, is adequately described by the following lumped parameter, truncated linear model (Preumont, 2002),

$$G_d(s) = e_a \frac{d}{f_a}(s) \approx \sum_{i=1}^{n_d} \frac{\beta_i}{s^2 + 2\zeta_i\omega_i s + {\omega_i}^2} + D_r \tag{2}$$

where n_d is the number of vibration modes included. Here, $\{\beta_i\}$ (m s^{-2} V^{-1}) are the control gains, $\{\zeta_i\}$ are the damping coefficients for each mode, and $\{\omega_i\}$ (rad s^{-1}) are the natural frequencies for the modes. The term D_r (m V^{-1}) is the residual mode, which is an approximation of the non-modeled higher frequency modes, and can be included to improve prediction of zero-locations. The addition of D_r produces a model that is not strictly proper, but as the instrumentation, such as the amplifier and sensors, have limited bandwidth, D_r can be considered equal to zero for this system. Eq. (2) has a pole-zero

interleaving property (Preumont, 2002), which is the origin of positive-realness (passivity) and negative-imaginariness for certain input-output pairs (Petersen and Lanzon, 2010). The inclusion of instrumentation dynamics, and sensor-actuator pairs that are not perfectly co-located, will in general invalidate the the pole-zero interleaving property (Preumont, 2002).

2.3 Charge

When applying passive shunt-damping, the induced charge in the actuator circuit is utilized. The charge in the actuator circuit can be found as (Eielsen and Fleming, 2010)

$$q = e_a d + C_p u_a = C_p(u_a + \alpha d) \ ,$$

where C_p (F) is the capacitance of the piezoelectric stack actuator, and α (V m^{-1}) is a constant determining the amount of voltage generated by the direct piezoelectric effect due to the displacement d of the mechanical structure. The transfer function from applied voltage u_a to induced charge q is therefore

$$G_q(s) = \frac{q}{u_a}(s) = C_p(1 + \alpha G_d(s)) \ . \tag{3}$$

2.4 Force Transducer

The integral force feedback scheme utilizes a co-located piezoelectric force transducer. The force transducer generates a charge, depending on the applied force. The current or charge produced by the force transducer is typically converted to a voltage signal using a simple op-amp circuit with a high input impedance. The output voltage from such a sensor when measuring the charge, can be found to be (Preumont, 2002)

$$v_f = k_s(d - k_f u_a) \ ,$$

where d is the displacement of the mechanical structure, u_a is the applied voltage to the actuator, k_f (m V^{-1}) is the gain of the feed-through term, and k_s (V m^{-1}) is the sensor gain. The transfer-function from applied voltage u_a to measured sensor voltage v_f can therefore be found as

$$G_f(s) = \frac{v_f}{u_a}(s) = k_s(G_d(s) - k_f) \ . \tag{4}$$

2.5 Identification and Uncertainty

In order to identify the parameters in (2), (3), and (4), the frequency responses for the displacement, charge, and force are recorded using a SR780 Dynamic Signal Analyzer from Stanford Research Systems, applying a 150-mV RMS bandwidth-limited white noise excitation signal. The models are fitted into the procured data using the MATLAB System Identification and Optimization Toolboxes. As the noise from the force transducer is orders of magnitude lower than the noise from the displacement sensor (Fleming, 2010), the frequency response for the displacement is inferred from (4). The frequency response obtained using the displacement sensor is used to find the parameters in (3) and (4). The responses for $G_d(s)$, $G_q(s)$, and $G_f(s)$ are displayed in Figs. 3a, 3c, and 3e, respectively. The identified parameter values are presented in Tab. 1. For the displacement model (2), three vibration modes, $n_d = 3$, are included. By inspection of Fig. 3a, it can be seen that the second mode at 1660 Hz is the dominant piston mode.

The uncertainty of the models can be quantified as unstructured multiplicative perturbations. Since the control schemes considered are either single-input-single-output (SISO), or single-input-multiple-output (SIMO), the uncertainty description of the models from the scalar input u_p to the output vector y_p has the form (Heath and Gayadeen, 2011)

$$y_{p_i} = G_i(s)(1 + \delta_i(s)\Delta_i(s))u_p \ ; \ \|\Delta_i(s)\| \leq 1 \ , \tag{5}$$

where i denotes the index into the output vector y_p, such that $G_i(s)$ corresponds to the transfer function from the input u_p to the output y_{p_i}, and $\delta_i(s)$ is the corresponding frequency dependent uncertainty weight. The uncertainty weights $\{\delta_i(s)\}$ are determined experimentally, for each of the outputs, and are presented in Figs. 3b, 3d, and 3f. Over-bounding weights were also found to introduce more conservativeness.

Table 1. Identified model parameters.

Displacement model (2)		
$\{\beta_1, \beta_2, \beta_3\}$	$\{1.80 \cdot 10^4, 2.54 \cdot 10^6, 4.83 \cdot 10^6\}$	μm s^{-2} V^{-1}
$\{\zeta_1, \zeta_2, \zeta_3\}$	$\{0.0726, 0.0196, 0.0312\}$	-
$\{\omega_1, \omega_2, \omega_3\}$	$\{2\pi \cdot 490, 2\pi \cdot 1660, 2\pi \cdot 3400\}$	rad s^{-1}
Charge model (3)		
C_p	195	nF
α	3.95	V μm^{-1}
Force model (4)		
k_s	$2.52 \cdot 10^{-7}$	V μm^{-1}
k_f	0.0451	μm V^{-1}

3. CONTROL DESIGN

The control schemes presented will be analyzed with regards to the general control structure shown in Fig. 4.

3.1 Performance Measures

The control schemes considered are either single-input-single-output (SISO), or single-input-multiple-output (SIMO). Considering the general SIMO case, it can be seen that for the control structure in Fig. 4, the control input is given as

$$u_p = C(s)(r - F(s)y_p) \ , \tag{6}$$

where $C(s)$ is a one-row feed-forward transfer-matrix, and $F(s)$ is a diagonal feedback transfer-matrix.

Breaking the loop at the error e of the one-column plant transfer-matrix $G_p(s)$, the loop transfer-matrix is

$$L(s) = F(s)G_p(s)C(s) \ ,$$

which defines the output sensitivity transfer-matrix $S_O(s)$ as

$$e = S_O(s)r = (I + L(s))^{-1}r \ , \tag{7}$$

where $e = r - F(s)y_p$. The complementary sensitivity transfer-matrix $T(s)$ becomes

$$y_p = T(s)r = G_p(s)C(s)S_O(s)r \ . \tag{8}$$

In addition, the transfer-matrix $N(s)$ from the additive sensor noise n to the output y_p is

$$y_p = N(s)n = -T(s)F(s)n \ , \tag{9}$$

and the transfer-matrix $E(s)$, measuring the deviation of the plant output y_p from the reference trajectory r, $\epsilon = r - y_p$, is

$$\epsilon = E(s)r = (I - T(s))r \ . \tag{10}$$

Note that $\epsilon \neq e$, if $F(s) \neq I$.

Breaking the loop at the input u_p of the plant, the loop transfer-matrix is

$$L_I(s) = C(s)F(s)G_p(s) \ ,$$

and the input sensitivity transfer-matrix $S_I(s)$ from the disturbance w to the input u_p is therefore

$$u_p = S_I(s)w = (I + L_I(s))^{-1}w \ , \tag{11}$$

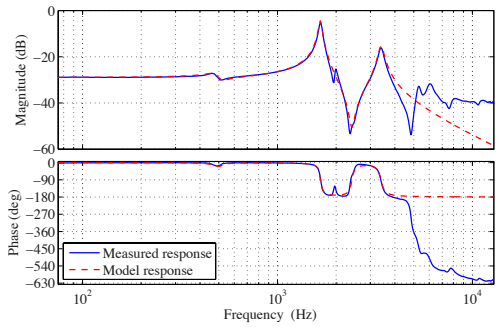

(a) Frequency response for the displacement model $G_d(s)$.

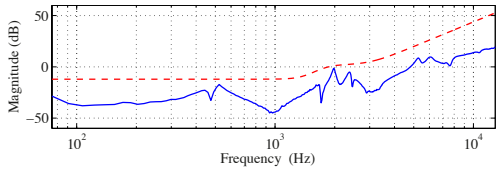

(b) Multiplicative uncertainty weight $\delta_d(s)$.

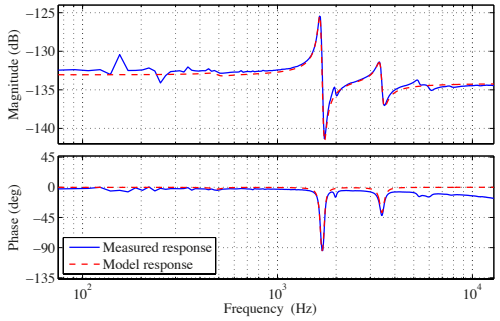

(c) Frequency response for the charge model $G_q(s)$.

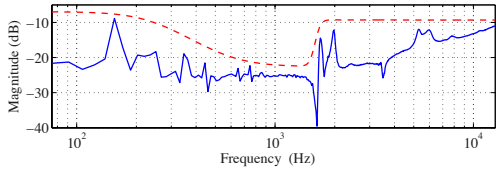

(d) Multiplicative uncertainty weight $\delta_q(s)$.

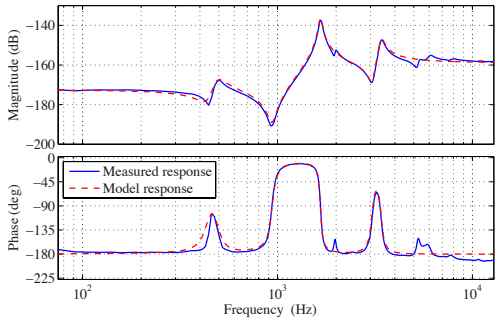

(e) Frequency response for the force model $G_f(s)$.

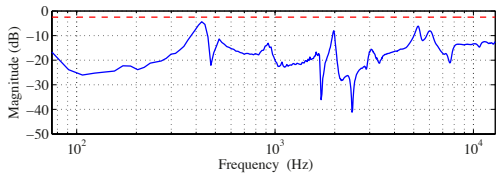

(f) Multiplicative uncertainty weight $\delta_f(s)$.

Fig. 3. Frequency responses and uncertainties.

which provides the transfer-matrix $D(s)$ from the disturbance w to the output y_p as

$$y_p = D(s)w = G_p(s)S_I(s)w \ . \tag{12}$$

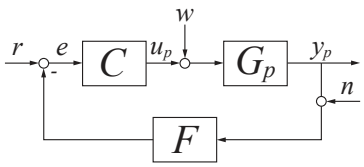

Fig. 4. General control structure.

The performance will be evaluated with regards to the flatness of the response of $T(s)$, the bandwidth of $E(s)$, the attenuation of the input disturbance w to the displacement d, and the amplification of sensor noise n to the displacement d. The bandwidth of $E(s)$ is defined as the frequency where $|E(j\omega)|$ first crosses the line of -3 dB from below at the frequency response diagram. At this frequency the tracking error ϵ is 50% of the reference r, thus there is effectively no tracking of frequency components above the bandwidth. The attenuation of the input disturbance is measured by the $\mathcal{H}_\infty$-norm, $\|D(s)\|_\infty$, which corresponds to the peak magnitude of $D(s)$. The added displacement noise is measured by the $\mathcal{H}_2$-norm, $\|N(s)\|_2$, which provides the root-mean-square displacement noise response if n is taken to be equal to unity variance Gaussian white noise. E.g., the displacement variance due to sensor noise can be found as ${\sigma_d}^2 = \|N(s)\|_2^2 {\sigma_n}^2$.

3.2 Robust Stability Measure

The SIMO robust stability criterion described in Heath and Gayadeen (2011), for multiplicative uncertainty on the form (5), can straight-forwardly be adapted to the control structure in Fig. 4. Robust stability can be ensured if

$$\sup_\omega \sum_{i=1}^{n_y} |S_I(j\omega)G_i(j\omega)C_i(j\omega)F_i(j\omega)\delta_i(j\omega)| = \gamma \leq 1 \ , \tag{13}$$

where the matrix elements $C_i(s)$ and $F_i(s)$ correspond to the output y_{p_i}, and n_y is the number of outputs. The inverse value of the norm, $1/\gamma$, provides a measure of the minimum amount of additional multiplicative uncertainty that the system can tolerate before it becomes unstable, for a given frequency weight, δ_i.

3.3 Tuning

Control design for fixed-structure, low-order control laws using output feedback is a long-standing and challenging problem in control engineering. A common approach to output feedback problems, is to use $\mathcal{H}_\infty$-synthesis. If the control law is allowed to have any order and every matrix of the control law is freely tunable, $\mathcal{H}_\infty$-synthesis guarantees a solution to the control design problem by convex optimization.

For a control law with a fixed structure and lower order than the plant, this approach can not be applied. There exist some results for fixed low-order control problems, solved with the use of linear matrix inequalities, but these methods do not allow for the use of unstructured uncertainty, do not guarantee global, and in many cases not even local, convergence, and might not accommodate for control laws where the structure is fixed in addition to the order (Syrmos et al., 1997; Ibaraki and Tomizuka, 2001). In other words, there does not exist any general control design method for output feedback using fixed-structure, low-order control laws. A practical optimization procedure is therefore proposed in order to obtain good tracking performance.

Control design is often a trade-off between conflicting goals. For nanopositioning systems, it is desirable to have a high bandwidth for $E(s)$ in order to have good reference tracking. Also, the system is required to well damped in order to avoid excessive vibrations. This translates to an absence of peaks in $T(s)$. To counter hysteresis and creep, as well as environmental disturbances, $D(s)$ must provide a high degree of attenuation. In addition, the amplification of sensor noise should be as small as possible, meaning that $N(s)$ should have the smallest bandwidth possible. Due to the restriction imposed by the Bode sensitivity integral (Goodwin et al., 2000), it is impossible to meet these criteria simultaneously.

As the purpose of damping control is to reduce peaks in the closed-loop response due to lightly damped vibration modes, and since ideal tracking performance is achieved when $d = r \Rightarrow T(s) = 1$, it appears that a good overall performance criterion is the flatness of $|T(j\omega)|$. Let θ_c be the vector of control law parameters. It is here proposed that the flatness criterion can be expressed using the cost function

$$J(\theta_c) = \| 1 - |T(\theta_c; j\omega)| \|_2 \ , \tag{14}$$

where $\| \cdot \|_2$ is the L^2-norm. The expression $1 - |T(\theta_c; j\omega)|$ is typically not square-integrable with respect to ω, thus the L^2-norm is truncated as needed in order to produce a finite value, , integrating over the domain $[0, \Omega]$, where $\Omega > 0$ is well above the bandwidth of the mechanical system.

For the control schemes presented in the following sections, a practical and straight-forward method to find control law parameters that provide good tracking performance for a particular scheme is then to solve

$$\theta_c{}^* = \arg\min_{\theta_c} J(\theta_c) \text{ s.t. } \mathrm{Re}\{\lambda_i\} \in \mathbb{R}^- \ \wedge \ \gamma < 1 \ , \tag{15}$$

where $\{\lambda_i\}$ is the set of eigenvalues for the closed-loop system. The optimization problem can be solved either by using an exhaustive grid search over a domain of reasonable control law parameter values, or by using an unstructured optimization algorithm, e.g. the Nelder-Mead method (Lagarias et al., 1998).

4. CONTROL SCHEMES

4.1 Positive Position Feedback (PPF)

Damping and tracking control using PPF (Fanson and Caughey, 1990) combined with an integral control law can be implemented using the control structure in Fig. 5. This is equivalent to the control scheme in Aphale et al. (2008). The damping control law consists of a low-pass filter with negative gain

$$C_d(s) = \frac{-k_d}{s^2 + 2\zeta_d \omega_d s + {\omega_d}^2} \ , \tag{16}$$

were $k_d > 0$ is the control law gain, ζ_d the damping coefficient and ω_d is the cut-off frequency. The tracking control law consists of an integrator with a negative gain, which will be inverted by the negative gain of the filter (16),

$$C_t(s) = \frac{-k_t}{s} \ . \tag{17}$$

Here, $k_t > 0$ is the gain of the integral term.

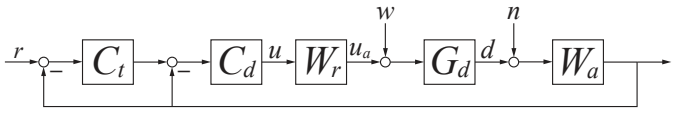

Fig. 5. Structure when using PPF and IRC.

To analyze the nominal performance of the control scheme, the control structure in Fig. 5 can be put on the equivalent formulation adhering to the control structure in Fig. 4. The feed-forward filter is found as

$$C(s) = W_r(s) C_d(s) C_t(s) \ , \tag{18}$$

and the feedback filter is found as

$$F(s) = W_a(s)(1 + C_t^{-1}(s)) \ . \tag{19}$$

Using the above expressions, and assuming

$$G_p(s) = G_d(s) \ ,$$

it is straight forward to find the transfer functions for the sensitivity (7), the complementary sensitivity (8), the noise attenuation (9), the error attenuation (10), and the disturbance rejection (12). Here, $W_r(s) = W_a(s)$, and are second-order Butterworth filters, with a cut-off frequency at 20 kHz.

The robust stability with regards to the multiplicative model uncertainty can be evaluated using the stability criterion (13), using (8), (18) and (19).

There are four tunable control law parameters

$$\theta_c = [k_d, \zeta_d, \omega_d, k_t]^{\mathrm{T}} \ ,$$

the feedback filter gain g_f, the damping ratio ζ_f, the cut-off frequency ω_f, and the tracking integral control law gain k_t. The optimal control law parameters for (16) and (17) found when solving (15) are

$k_d = 2.32{\cdot}10^8$, $\zeta_d = 0.564$, $\omega_d = 2\pi{\cdot}1470$, $k_t = 2.31{\cdot}10^4$.

The resulting nominal frequency responses for $T(S)$, $E(s)$, and $D(s)$ are shown in Fig. 9a.

4.2 Integral Resonant Control (IRC)

Damping and tracking control applying IRC (Aphale et al., 2007) to introduce damping can also be implemented using the control structure in Fig. 5. In this control scheme (Fleming et al., 2010) the damping control law is

$$C_d(s) = \frac{-k_d}{s - k_d D_f} \ . \tag{20}$$

Eq. (20) is the result of rearranging the IRC scheme to a form suitable for tracking control (Fleming et al., 2010). Here $k_d > 0$ is the integral damping gain, while D_f is a feedthrough term. In addition, the tracking control law is

$$C_t(s) = \frac{-k_t}{s} \ , \tag{21}$$

where $k_t > 0$ is the gain of the integral term.

As this scheme uses the same structure as the one based on PPF in Section 4.1, the scheme can be analyzed using the same equivalent formulation with regards to the general control structure in Fig. 4, i.e., with

$$C(s) = W_r(s) C_d(s) C_t(s) \tag{22}$$

and

$$F(s) = W_a(s)(1 + C_t^{-1}(s)) \ . \tag{23}$$

Here, $W_r(s) = W_a(s)$, and are second-order Butterworth filters, with a cut-off frequency at 20 kHz.

For this scheme, there are three tunable control parameters

$$\theta_c = [D_f, k_d, k_t]^{\mathrm{T}} \ ,$$

the feedthrough term D_f, the integral damping gain k_d, and the tracking integral control law gain k_t. The optimal control law parameters for (20) and (21) found when solving (15) are

$$D_f = -0.116 \ , \ k_d = 8.75 \cdot 10^4 \ , \ k_t = 7.12 \cdot 10^3 \ .$$

The resulting nominal frequency responses for $T(S)$, $E(s)$, and $D(s)$ are shown in Fig. 9b.

4.3 Integral Force Feedback (IFF)

The dual-sensor damping and tracking control scheme proposed in Fleming (2010), is based on IFF (Preumont et al., 1992), and can be implemented using the control structure shown in Fig. 6, where $G_f(s)$ is as described in (4).

The advantage of using this scheme, is that the piezoelectric force transducer has a noise density orders of magnitude lower than a capacitive probe, thus allowing high bandwidth, but with substantially lower displacement noise due to feedback. The drawback is reduced range, as the force sensor replaces parts of the actuator, and additional instrumentation to amplify the charge generated by the transducer. The force sensor also requires good calibration, and the response is slightly non-linear, but this is an insignificant source of error at higher frequencies.

The control scheme requires an integral control law,

$$C_i(s) = \frac{k_i}{s} \,, \tag{24}$$

to be implemented, where $k_i > 0$ is the gain. In addition, two splitting filters, a low-pass and a high-pass filter, must be implemented. The low-pass filter is given as

$$W_{lp}(s) = \frac{\omega_f}{s + \omega_f} \,, \tag{25}$$

while the high-pass filter is given as

$$\lambda W_{hp}(s) = \lambda \frac{s}{s + \omega_f} \,, \tag{26}$$

where the gain λ is found as

$$\lambda = |G_d(0)/G_f(0)| \,. \tag{27}$$

The cut-off frequency ω_f determines the split between the frequency range for where to use displacement feedback, and where to use force feedback. For the implementation, this was chosen to be $\omega_f = 2\pi \cdot 50$. Better noise properties can be achieved by reducing ω_f, but this is limited to some extent by the need to high-pass filter the force measurement. The high-pass filter is used both to allow the use of the capacitive probe measurement at low frequencies, and to remove bias components in the charge measurement. As the force transducer response is slightly non-linear, sufficient bandwidth for the capacitive probe measurement is required to improve linearity.

This is a single-input-multiple-output (SIMO) system, and the measurement vector is given as

$$y_p = [d,\ v_f]^{\mathrm{T}} \,, \tag{28}$$

while the input is the applied voltage u_a. With regards to Fig. 4, the plant transfer-matrix is

$$G_p(s) = [G_d(s),\ G_f(s)]^{\mathrm{T}} \in \mathbb{C}^{2\times 1} \,, \tag{29}$$

the feed-forward transfer-matrix is given as

$$C(s) = [W_r(s)C_i(s),\ -W_r(s)C_i(s)] \,, \tag{30}$$

and the feedback transfer-matrix is given as

$$F(s) = \mathrm{diag}\big(W_{lp}(s)W_a(s)\,,\ \lambda W_{hp}(s)W_a(s)\big) \,. \tag{31}$$

Here, $W_r(s) = W_a(s)$, and are second-order Butterworth filters, with a cut-off frequency at 20 kHz.

There is one tunable control parameter

$$\theta_c = k_i \,,$$

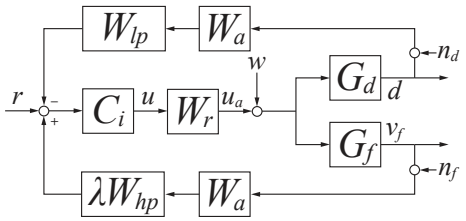

Fig. 6. Structure when using IFF.

the integral gain k_i. The optimal control law parameter for (24) found when solving (15) is

$$k_i = 1.37 \cdot 10^5 \,.$$

It can also be found using a root-locus plot. The resulting nominal frequency responses for $T(S)$, $E(s)$, and $D(s)$ are shown in Fig. 9c.

4.4 Passive Shunt-Damping (PSD)

PSD (Hagood and von Flotow, 1991) can introduce damping by adding an inductor and a resistor in series with the piezoelectric actuator, which acts as a capacitor, due to the large dielectric constant of the piezoelectric material. Tuning the resulting LCR-circuit for maximum damping creates a resonant LCR-circuit that works analogously to a tuned mechanical absorber. Adding an integral control law for tracking, results in the control structure shown in Fig. 7, where $G_q(s)$ is as given in (3). As discussed below, this configuration does not result in the same tuning of the LCR-circuit as would be the case when optimizing for maximum damping only.

The transfer function for the added shunt is (Eielsen and Fleming, 2010)

$$Z(s) = sL + R \,, \tag{32}$$

where L (H) is the inductance, and R (Ω) is the resistance. The integral control law is

$$C_i(s) = \frac{k_i}{s} \,, \tag{33}$$

where $k_i > 0$ is the gain.

This can be interpreted as a single-input-multiple-output (SIMO) system, where the measurement vector is given as

$$y = [d,\ v_f]^{\mathrm{T}} \tag{34}$$

and the input is the applied voltage u_a. With regards to Fig. 4, the plant transfer-matrix is

$$G(s) = [G_d(s),\ G_q(s)]^{\mathrm{T}} \in \mathbb{C}^{2\times 1} \,, \tag{35}$$

the feed-forward transfer-matrix is

$$C(s) = [W_r(s)C_i(s),\ sZ(s)] \,, \tag{36}$$

and the feedback transfer-matrix is given by

$$F(s) = \mathrm{diag}\big(W_a(s)\,,\ 1\big) \,. \tag{37}$$

Here, $W_r(s) = W_a(s)$, and are second-order Butterworth filters, with a cut-off frequency at 20 kHz.

There are three tunable control parameters

$$\theta_c = [L, R, k_i]^{\mathrm{T}} \,,$$

the shunt inductance L, the shunt resistance R, as well as the tracking integral control law gain k_i. The optimal control law parameters for (32) and (33) found when solving (15) are

$$L = 49.5\ \mathrm{mH} \,,\ R = 613\ \Omega \,,\ k_i = 7.50 \cdot 10^4 \,.$$

The resulting nominal frequency responses for $T(S)$, $E(s)$, and $D(s)$ are shown in Fig. 9d.

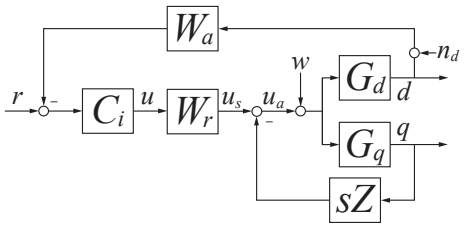

Fig. 7. Structure when using PSD.

It should be noted that the values for L and R found using (15) are not the same as when optimizing for maximum damping. In that case $L = 46.6$ mH and $R = 165\ \Omega$, which produces a resonant LCR-circuit response due to the much smaller resistance value. Since

$$\bar{G}_d(s) = \frac{d}{u_s}(s) = \frac{G_d(s)}{1 + sZ(s)G_q(s)} = W_s(s)G_d(s)$$

when the shunt is present, the source voltage u_s is filtered by $W_s(s)$ before it is applied to the actuator. The response obtained for $W_s(s)$ when using the values of L and R found when solving (15) is almost identical to that of a Butterworth filter with cut-off frequency $\omega_c = \sqrt{1/LC_p}$, although there is still some additional damping introduced due to the $\alpha G_d(s)$ term in (3). This means that the shunt can be approximated by a second-order low-pass Butterworth filter, as done in Sec. 4.5.

The shunt was implemented using an inductor constructed using a closed ferrite core and approximately 45 turns of copper wire. A potentiometer was used to implement the required resistance. The inductor and resistor were tuned to their required values using an Agilent U1733C LCR meter.

4.5 Damping Integral Control (DI)

As noted in Sec. 4.4, the optimal values for the resistance and inductance for the shunt result in a low-pass filter when connected to the capacitance of the actuator, with approximately the same response as a second-order low-pass Butterworth filter. Implementing a control scheme on a microcontroller or a computer, reconstruction and anti-aliasing filters must be present in order to avoid aliasing and reduce quantization noise. Instead of applying a shunt circuit, the reconstruction and anti-aliasing filters that are already present as part of the instrumentation can be used. The resulting control structure is shown in Fig. 8, and corresponds to the scheme presented in Eielsen et al. (2011).

As when using passive shunt-damping, only an integral control law needs to be implemented, i.e.,

$$C_i(s) = \frac{k_i}{s}\ , \tag{38}$$

where $k_i > 0$ is the gain. The cut-off frequency, ω_c, for the filters $W_r(s)$ and $W_a(s)$ must be tuned as well. Here it is assumed that $W_r(s) = W_a(s)$ for simplicity. The filters used in the experimental set-up are second-order Butterworth filters,

$$W_r(s) = W_a(s) = {\omega_c}^2/(s^2 + \sqrt{2}\omega_c s + {\omega_c}^2)\ . \tag{39}$$

The combined filter $W_r(s)W_a(s)$ is of fourth-order, but the closed-loop response of the system is almost identical to the case when using a passive shunt. The added benefit in this case is that the shunt is no longer needed.

Formulating the control scheme in terms of the general control structure in Fig. 4, the feed-forward filter is

$$C(s) = W_r(s)C_i(s) \tag{40}$$

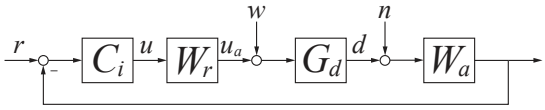

Fig. 8. Structure when introducing damping by applying a low-pass filter in the signal chain, in this case by utilizing the filter $W_r(s)W_a(s)$.

and the feedback filter is

$$F(s) = W_a(s)\ . \tag{41}$$

There are two tunable control parameters

$$\theta_c = [\omega_c, k_i]^{\mathrm{T}}\ ,$$

the filter cut-off frequency ω_c, and the tracking integral control law gain k_i.The optimal control law parameters for (38) and (39) found when solving (15) are

$$\omega_c = 2\pi \cdot 2150\,,\ k_i = 6.68 \cdot 10^4\,.$$

The resulting nominal frequency responses for $T(S)$, $E(s)$, and $D(s)$ are shown in Fig. 9e.

5. EXPERIMENTAL RESULTS AND DISCUSSION

The five different control schemes were implemented on the hardware-in-the-loop system, described in Sec. 2, and the tracking performance when using a triangle wave reference signal with a fundamental frequency of 80 Hz and an amplitude of 1 μm is recorded for each scheme. The fundamental frequency of the reference signal is chosen in order for the 21st harmonic of the signal to be close to the dominant vibration mode. The displacement for all the schemes is measured on a separate channel using an anti-aliasing filter with a 35 kHz cut-off frequency. The generated current from the force transducer is measured, and integrated numerically. The cut-off frequency for the anti-aliasing filter for this measurement is always 20 kHz, for all the experiments.

Nominal frequency responses for the various schemes are found in Figs. 9a, 9b, 9c, 9d, and 9e. The measures from Sec. 3 are summarized in Tab. 2. Note that the values for $1/\gamma$ are not directly comparable between SISO and SIMO systems.

The results when tracking a triangle-wave reference signal are presented in Fig. 10. The maximum error (ME) ranges from 15% to 24%, and the root-mean-square error (RMSE) ranges from 0.11 μm to 0.20 μm. The error values are also summarized in Tab. 2. Note that tracking performance can be increased by adding feed-forward, but this is not done in order for the error signals to be significantly larger than the noise in the measured displacement signal, to avoid obfuscating the actual results achieved due to feedback.

Table 2. Bandwidth (BW) of $E(s)$, $||N(s)||_2$ from n_d to d, $||D(s)||_\infty$ from w to d, $1/\gamma$, root-mean-square error (RMSE), and maximum error (ME).

Scheme	BW	$\|\|N(s)\|\|_2$	$\|\|D(s)\|\|_\infty$	$1/\gamma$	RMSE	ME
PPF	318 Hz	61.1	$191{\cdot}10^{-3}$	1.66	0.194 μm	0.231 μm
IRC	369 Hz	78.4	$281{\cdot}10^{-3}$	1.01	0.173 μm	0.213 μm
IFF	329 Hz	12.6	$424{\cdot}10^{-4}$	1.14	0.123 μm	0.146 μm
PSD	338 Hz	60.0	$139{\cdot}10^{-3}$	1.14	0.178 μm	0.218 μm
DI	372 Hz	58.6	$204{\cdot}10^{-3}$	1.66	0.197 μm	0.235 μm

The best performing control schemes in terms of the error is the scheme using IFF. The worst performance is obtained when using PPF and the DI scheme, while when using IRC and PSD, errors in the middle of the range are obtained.

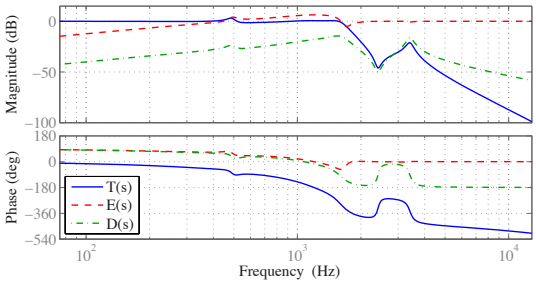

(a) Positive position feedback (PPF).

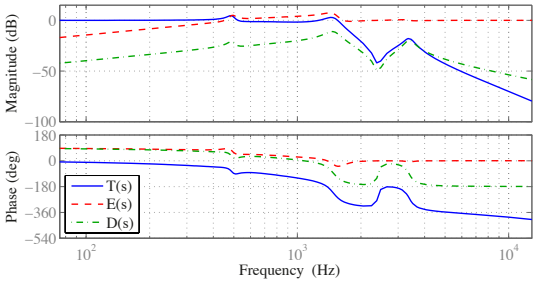

(b) Integral resonant control (IRC).

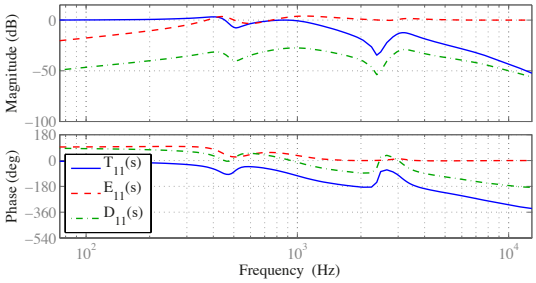

(c) Integral force feedback (IFF).

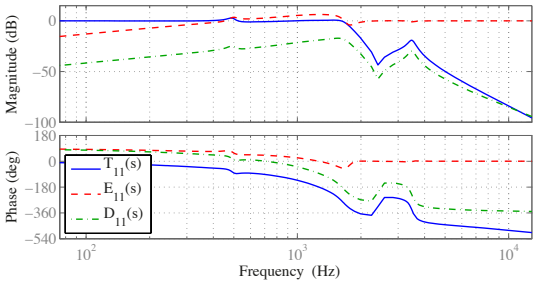

(d) Passive shunt-damping (PSD).

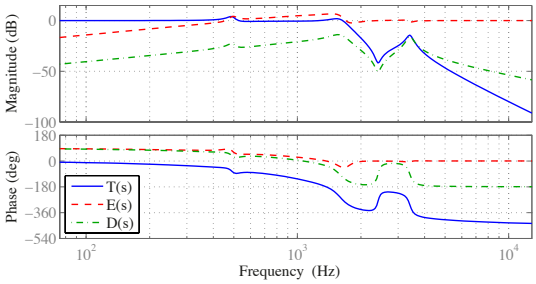

(e) Damping integral control (DI).

Fig. 9. Nominal frequency responses.

The error figures in terms of ME and RMSE can be changed by the control law tuning, but a reduction in RMSE typically leads to an increase in ME, due to a more oscillatory response.

The simplest control schemes to implement on a digital platform are the PSD based and DI schemes, as they only require a single integrator. The DI scheme is the simplest with regards to extra instrumentation, as it is not necessary to add a shunt circuit, although for the PSD based control law, the anti-aliasing filter is not necessary, and can be omitted. For an analog implementation, the DI scheme, and the schemes based on PPF, IRC, and PSD are almost equivalent in terms of complexity. The IFF based scheme also only requires three integrators in the implementation, but has the disadvantage of reduced range due to the force transducer, and it requires more instrumentation and good calibration. On the other hand, the noise performance is superior, due to the extremely low noise density of the force transducer, although this benefit is lost for a digital implementation, due to quantization noise and digital-to-analog converter (DAC) artifacts.

As quantization noise is the dominant noise source in the experimental system, it is not possible to obtain reliable closed-loop noise measurements. However, due to the low noise and high sensitivity of the force transducer, the effect of quantization noise and DAC artifacts can be measured. An example of this is shown in Fig. 11, where the time derivative of the force measurement is shown when using the IFF based scheme and the PSD scheme. The PSD scheme, as well as the DI scheme, has a low-pass filter with a low cut-off frequency before the voltage is applied to the piezoelectric actuator, and so the noise and disturbances coming from the DAC are effectively attenuated. For the PPF, IRC, and IFF based schemes, the reconstruction filter has a cut-off frequency of 20 kHz, and thus the non-ideal DAC behavior is much more noticeable. This beneficial effect can also be achieved when using PPF and IRC schemes by implementing the damping control law $C_d(s)$ using analog components, as it takes the form of a low-pass filter in either case, but implementing the whole scheme using analog components by adding an analog integrator might then be a better option.

Overall, the performance is fairly similar among the five schemes, but the excellent nominal noise performance of the IFF based scheme and the simplicity of the DI scheme is noteworthy.

Table 3. Feature summary.

	PPF	IRC	IFF	DI	PSD
Suitable for digital implementation				•	•
Low implementation complexity		•		•	
High overall performance and robustness			•		

6. CONCLUSIONS

Five fixed-structure, low-order control schemes for damping and tracking control for a nanopositioning device have been presented, experimentally assessed, and compared with regards to performance. Investigated schemes were based on PPF, IRC, IFF, and PSD, in addition to DI. The paper furthermore presented a practical and systematic tuning method for the schemes.

Overall, the performance was fairly similar among the schemes, but features of notice is the noise performance of the IFF based scheme and the simplicity of the DI scheme. It was demonstrated that when implementing control schemes on a digital platform, it is beneficial to use control schemes that reduce the effect of quantization noise and digital-to-analog-converter artifacts by using low-pass filters with low cut-off frequencies before the input to the actuator. Of the schemes investigated, this is most easily done using the PSD based scheme and the DI scheme. It was also demonstrated that the noise benefits when

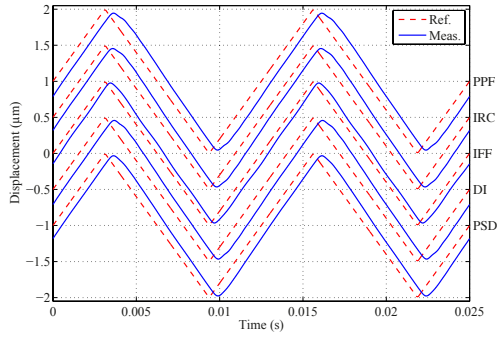

(a) Displacement measurement signals and reference signal.

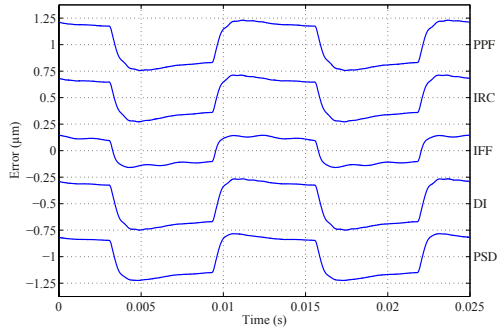

(b) Error signals.

Fig. 10. Steady-state tracking performance when applying a 1 μm amplitude, 80 Hz triangle-wave reference signal.

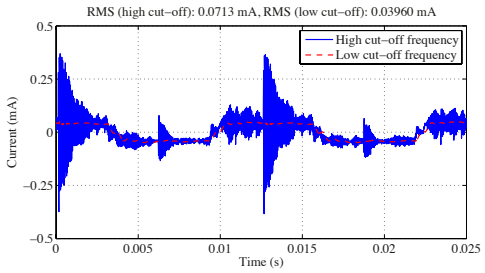

Fig. 11. Time derivative of force measurement; effect of filtering on DAC artifacts in the applied voltage when using a filter with high vs. low cut-off frequency.

using the IFF based scheme are lost for a digital implementation, due to quantization noise and digital-to-analog converter artifacts. Tab. 3 summarizes some of these features.

REFERENCES

Aphale, S.S., Bhikkaji, B., and Moheimani, S.O.R. (2008). Minimizing Scanning Errors in Piezoelectric Stack-Actuated Nanopositioning Platforms. *IEEE Trans. Nanotechnol.*, 7(1), 79–90.

Aphale, S.S., Fleming, A.J., and Moheimani, S.O.R. (2007). Integral Resonant Control of Collocated Smart Structures. *Smart Mater. Struct.*, 16(2), 439–446.

Bertotti, G. and Mayergoyz, I.D. (2005). *The Science of Hysteresis*, volume 3 of *Mathematical modeling and applications*. Academic Press, 1st edition.

Clayton, G.M., Tien, S., Leang, K.K., Zou, Q., and Devasia, S. (2009). A Review of Feedforward Control Approaches in Nanopositioning for High-Speed SPM. *J Dyn Syst-T ASME*, 131(6), 061101 (19 pages).

Devasia, S., Eleftheriou, E., and Moheimani, S.O.R. (2007). A Survey of Control Issues in Nanopositioning. *IEEE Trans. Control Syst. Technol.*, 15(5), 802–823.

Eielsen, A.A., Burger, M., Gravdahl, J.T., and Pettersen, K.Y. (2011). PI2-Controller Applied to a Piezoelectric Nanopositioner Using Conditional Integrators and Optimal Tuning. In *Proc. 18th IFAC World Congr.*, 887–892. Milano.

Eielsen, A.A. and Fleming, A.J. (2010). Passive Shunt Damping of a Piezoelectric Stack Nanopositioner. In *Proc. Amer. Contr. Conf.*, 4963–4968. Baltimore, MD.

Fanson, J.L. and Caughey, T. (1990). Positive Position Feedback-Control for Large Space Structures. *AIAA J*, 28(4), 717–724.

Fleming, A.J. (2010). Nanopositioning System With Force Feedback for High-Performance Tracking and Vibration Control. *IEEE/ASME Trans. Mechatronics*, 15(3), 433–447.

Fleming, A.J., Aphale, S., and Moheimani, S.O.R. (2010). A New Method for Robust Damping and Tracking Control of Scanning Probe Microscope Positioning Stages. *IEEE Trans. Nanotechnol.*, 9(4), 438–448.

Goodwin, G.C., Graebe, S.F., and Salgado, M.E. (2000). *Control System Design*. Prentice Hall.

Hagood, N.W. and von Flotow, A. (1991). Damping of structural vibrations with piezoelectric materials and passive electrical networks. *J. Sound Vibrat.*, 146(2), 243–268.

Heath, W.P. and Gayadeen, S. (2011). Simple robustness measures for control of MISO and SIMO plants. In *Proc. 18th IFAC World Congr.*, 11356–11361. Milano.

Ibaraki, S. and Tomizuka, M. (2001). Tuning of a Hard Disk Drive Servo Controller Using Fixed-Structure Hinf Controller Optimization. *J Dyn Syst-T ASME*, 123(3), 544–560.

Ioannou, P.A. and Sun, J. (1995). *Robust Adaptive Control*. Prentice Hall.

Lagarias, J., Reeds, J., Wright, M., and Wright, P. (1998). Convergence properties of the Nelder-Mead simplex method in low dimensions. *SIAM J. Optimiz.*, 9(1), 112–147.

Leang, K.K. and Fleming, A.J. (2009). High-speed serial-kinematic SPM scanner: design and drive considerations. *Asian J Control*, 11(2), 144–153.

Lyons, R.G. (2010). *Understanding Digital Signal Processing*. Prentice Hall, 3nd edition.

Newcomb, C.V. and Flinn, I. (1982). Improving the Linearity of Piezoelectric Ceramic Actuators. *Electron. Lett.*, 18(11), 442–444.

Petersen, I. and Lanzon, A. (2010). Feedback Control of Negative-Imaginary Systems. *IEEE Control Syst. Mag.*, 30(5), 54–72.

Pota, H., Moheimani, S.O.R., and Smith, M. (2002). Resonant Controllers for Smart Structures. *Smart Mater. Struct.*, 11(1), 1–8.

Preumont, A. (2002). *Vibration Control of Active Structures*. Kluwer Academic, 2nd edition.

Preumont, A. (2006). *Mechatronics*. Springer.

Preumont, A., Dufour, J., and Malekian, C. (1992). Active Damping by a Local Force Feedback with Piezoelectric Actuators. *J. Guid. Control Dynam.*, 15(2), 390–395.

Salapaka, S.M. and Salapaka, M.V. (2008). Scanning Probe Microscopy. *IEEE Control Syst. Mag.*, 28(2), 65–83.

Skogestad, S. and Postlethwaite, I. (2005). *Multivariable Feedback Control*. Wiley-Interscience.

Stepanenko, Y. and Su, C.Y. (1998). Intelligent Control of Piezoelectric Actuators. In *Proc. 37th IEEE Decis. Contr.*, 4234–4239. Tampa, FL.

Syrmos, V., Abdallah, C., Dorato, P., and Grigoriadis, K. (1997). Static Output Feedback—A Survey. *Automatica*, 33(2), 125–137.